

## HIGH-REYNOLDS NUMBER VISCOUS FLOW COMPUTATIONS USING AN UNSTRUCTURED-GRID METHOD

Hong Luo and Joseph D. Baum  
Science Applications International Corporation  
1710 SAIC Drive, MS 2-6-9  
McLean, VA 22102, USA

and

Rainald Löhner  
Institute for Computational Sciences and Informatics  
George Mason University, Fairfax, VA 22030, USA

### ABSTRACT

An unstructured grid method is presented to compute three-dimensional compressible turbulent flows for complex geometries. The Navier-Stokes equations along with the one equation turbulence model of Spalart-Allmaras are solved using a parallel, matrix-free implicit method on unstructured tetrahedral grids. The developed method has been used to predict drags in the transonic regime for both DLR-F4 and DLR-F6 configurations to assess the accuracy and efficiency of the method. The results obtained are in good agreement with experimental data, indicating that the present method provides an accurate, efficient, and robust algorithm for computing turbulent flows for complex geometries on unstructured grids.

### 1. INTRODUCTION

Computational fluid dynamics (CFD) has become an indispensable tool for the aerodynamic design and analysis of aircrafts and engines. The difficulty of generating structured grids and the desire to compute flows over increasingly complex configurations has fueled interest in the development of unstructured grid methods. Unstructured grids provide great flexibility in tackling complex geometries encountered in practice and offer a natural framework for adapting to flow features. Nowadays, unstructured grids composed of geometric simplices, i.e., triangle in two dimensions and tetrahedra in three dimensions are widely and routinely used for producing high-quality solutions for both inviscid flows and low Reynolds number viscous flows. However, so far, the solution of the Navier-Stokes equations for high Reynolds number viscous flows has been dominated by structured grid methods, as grid stretching along shear layers is a trivial task on structured meshes but is relatively difficult to achieve on unstructured triangular or tetrahedral grids. One popular approach

has been to use a hybrid grid: prismatic elements are used for viscous regions where the grid is highly stretched, and tetrahedral elements for inviscid regions where the grid is nearly isotropic<sup>1-3</sup>. Although this approach seems to be attractive, the need to generate a prismatic grid unavoidably renders the grid generation more difficult and less robust for complex geometries, which would otherwise has been the main advantage of unstructured grid methods. In fact, one can easily show that the prismatic grid generator will fail for the corners, where the newly created point is not visible from all the faces surrounding the original point<sup>4</sup>. Furthermore, the existence of several cell types in a hybrid grid undoubtedly makes mesh generation and adaptation, flow solution, and post-processing more complex.

The present authors have developed a parallel, accurate, fast, matrix-free implicit method to solve compressible turbulent flow problems using the Spalart and Allmaras one equation turbulence model on unstructured meshes<sup>5</sup>. In this method, the mean-flow and turbulence-model equations are decoupled in the time integration in order to facilitate the incorporation of different turbulence models and reduce memory requirements. Both mean flow and turbulent equations are integrated in time using a linearized implicit scheme. A fast, matrix-free implicit method, GMRES+LU-SGS<sup>6-8</sup>, is then applied to solve the resultant system of linear equations. The spatial discretization is carried out using a hybrid finite volume and finite element method, where the finite volume approximation based on a containment dual control volume rather than on the more popular median-dual control volume is used to discretize the inviscid fluxes, and the finite element approximation is used to evaluate the viscous flux terms. The parallelization of the unstructured implicit solver is achieved using OpenMP compiler directives on shared-memory, cache-based parallel machines<sup>9</sup>. The developed method has been used to compute a variety of compressible turbulent flow problems over a wide range of flow conditions. The computational results

demonstrated that this unstructured tetrahedral grid method is able to produce same quality solutions as its hybrid counterpart.

The objective of the effort discussed in this paper is to further assess performance of this unstructured grid method in regard to the numerical accuracy and computational efficiency for its ability to predict drag for complex geometries. Any flow solvers must undergo extensive validation and verification process, before they can be trusted and used as a design tool for predicting aerodynamic force coefficients such as lift, drag, and moments. This is especially crucial for drag prediction, as it is widely acknowledged that the computational method should be able to predict drag to within several counts, in order to be useful to an airplane designer. AIAA Applied Aerodynamics Technical Committee has organized two Drag Prediction Workshops held in Anaheim CA, June 2001, and Orlando FL, June 2003, respectively in order to assess the predictive capabilities of a number of state-of-the-art computational fluid dynamics methods. The test cases presented in these workshops provide an excellent database for evaluation of the existing computer codes using Navier-Stokes solvers. The current paper addresses results obtained for some test cases in these workshops. A good predictive ability of our unstructured grid method is demonstrated over a wide range of flow conditions, although accuracy is found to degrade for cases where increasing amounts of flow separation occur. It is also shown that with the significant advances of the current numerical method, turnaround within hours for numerical simulation of high Reynolds number turbulent flows around complex geometries has become a reality.

## 2. GOVERNING EQUATIONS

The Reynolds-averaged Navier-Stokes equations governing unsteady compressible viscous flows can be expressed in the conservative form as

$$\frac{\partial \mathbf{U}}{\partial t} + \frac{\partial \mathbf{F}^j}{\partial \mathbf{x}_j} = \frac{\partial \mathbf{G}^j}{\partial \mathbf{x}_j}, \quad (2.1)$$

where the summation convention has been employed. The flow variable vector  $\mathbf{U}$ , inviscid flux vector  $\mathbf{F}$ , and viscous flux vector  $\mathbf{G}$ , are defined by

$$\mathbf{U} = \begin{pmatrix} \rho \\ \rho u_i \\ \rho e \end{pmatrix}, \mathbf{F}^j = \begin{pmatrix} \rho u_j \\ \rho u_i u_j + p \delta_{ij} \\ u_j (\rho e + p) \end{pmatrix}, \quad (2.2)$$

$$\mathbf{G}^j = \begin{pmatrix} 0 \\ \sigma_{ij} \\ u_i \sigma_{lj} + q_j \end{pmatrix}.$$

Here  $\rho$ ,  $p$ , and  $e$  denote the density, pressure, and specific total energy of the fluid, respectively, and  $u_i$  is the velocity of the flow in the coordinate direction  $x_i$ .

The pressure can be computed from the equation of state

$$p = (\gamma - 1)\rho(e - \frac{1}{2}u_j u_j), \quad (2.3)$$

which is valid for perfect gas, where  $\gamma$  is the ratio of the specific heats. The components of the viscous stress tensor  $\sigma_{ij}$  and the heat flux vector are given by

$$\sigma_{ij} = (\mu + \mu_t)\left(\frac{\partial u_i}{\partial x_j} + \frac{\partial u_j}{\partial x_i}\right) - \frac{2}{3}(\mu + \mu_t)\frac{\partial u_k}{\partial x_k}\delta_{ij}, \quad (2.4)$$

$$q_j = \frac{1}{\gamma - 1}\left(\frac{\mu}{Pr} + \frac{\mu_t}{Pr_t}\right)\frac{\partial T}{\partial x_j}. \quad (2.5)$$

In the above equations,  $T$  is the temperature of the fluid,  $Pr$  the laminar Prandtl number, which is taken as 0.7 for air, and  $Pr_t$  the turbulent Prandtl number, which is taken as 0.9.  $\mu$  represents the molecular viscosity, which can be determined through Sutherland's law

$$\frac{\mu}{\mu_0} = \left(\frac{T}{T_0}\right)^{\frac{3}{2}}\frac{T_0 + S}{T + S}. \quad (2.6)$$

$\mu_0$  denotes the viscosity at the reference temperature  $T_0$ , and  $S$  is a constant which for air assumes the value  $S=110^\circ\text{K}$ . The temperature of the fluid  $T$  is determined by

$$T = \gamma\frac{p}{\rho}, \quad (2.7)$$

and  $\mu_t$  denotes the turbulence eddy viscosity, which is computed using Spalart and Allmaras one equation turbulence model<sup>10</sup>

$$\mu_t = \rho\tilde{\nu}f_{v1}. \quad (2.8)$$

The system is closed by including the governing equation for the working variable  $\tilde{\nu}$ , which can be written as

$$\frac{D\tilde{\nu}}{Dt} = \frac{1}{\sigma}\nabla \cdot ((\nu + (1 + c_{b2})\tilde{\nu})\nabla\tilde{\nu}) - \frac{c_{b2}}{\sigma}\tilde{\nu}\nabla\tilde{\nu} + c_{b1}(1 - f_{t2})\tilde{S}\tilde{\nu} - (c_{w1}f_w - \frac{c_{b1}}{\kappa^2}f_{t2})\left(\frac{\tilde{\nu}}{d}\right)^2. \quad (2.9)$$

The constants appearing in the above equations take on the standard values recommended in Ref. 10.

## 3. NUMERICAL METHOD

The numerical algorithms for solving the governing equations (2.1) and (2.9) are based on a loosely coupled approach. In this approach, the flow and turbulence variables are updated separately. At each time step, the flow equations (2.1) are solved first using the previously updated turbulent eddy viscosity. The turbulent equation (2.9) is then solved using the newly updated flow variables to advance the turbulence variable in time. Such a loosely coupled approach allows for the easy interchange of new turbulence models. Another advantage of this approach is that all the working arrays used to solve the flow

equations can be used to solve the turbulence equation. As a result, no additional storage is needed for the present implementation.

While unstructured grids are widely and routinely used for producing high-quality solutions for inviscid flow simulations, the development and application of simplicial unstructured grids to viscous flow simulations are far less popular, acceptable, and successful. For high Reynolds number viscous flows, the velocity variations in the normal direction are much larger than those in the tangential direction in the boundary layer and wake regions. This requires the use of the highly stretched meshes to efficiently resolve such viscous regions. For simplicial elements, this stretching invariably leads to the use of long and thin triangular cells. Numerical evidence, as reported by Aftosmis et al.<sup>11</sup>, Haselbacher et al.<sup>3</sup>, and Viozat et al.<sup>12</sup>, indicates that for the discretization of the inviscid fluxes, the classic 1D-based upwind schemes using median-dual finite volume approximation suffer from excessive numerical diffusion due to such skewing. This is mainly due to the presence of diagonal connections, where the right and left state data required for the upwind schemes are not well aligned with the normal to the interface. Two general options exist for solving this problem: scheme-based methods and mesh-based methods. The former approach attempts to develop multidimensional upwind methods that are based more deeply on physical aspects of the Euler equations. Several efforts have been made in this direction<sup>13–18</sup>. Among them are rotated upwind methodologies, multidimensional wave decomposition methods, and characteristic theory-based advection schemes. Despite much progress, numerical investigations have shown that none of these methods have yet reached a satisfactory level with respect to their accuracy and robustness. The latter approach is based on improving of the grids. The typical example of this approach is to use hybrid grids<sup>1–3</sup>, where the cell shapes, which do not become skewed with stretching (e.g., hexahedral and prisms), are used in the viscous regions and tetrahedral cells away from viscous regions. However, this is not completely satisfactory from the application point of view, as the existence of several cell types in a hybrid grid undoubtedly makes mesh generation and adaptation, flow solution, and post-processing more complex. Alternatively, one could use a containment dual finite volume approximation<sup>5,12,19</sup>, which significantly reduces the influence of the diagonal edges in the grid. In fact, one can show that the resulting control volume on an ideal triangulated quadrilateral grid using such containment dual is essentially identical to the control volume on the quadrilateral grid using a median control volume. Our experience<sup>5</sup> has shown that using containment dual-based finite volume approxi-

mation, simplicial unstructured grids can be applied to accurately compute high Reynolds number viscous flows and produce same quality solutions as its hybrid counterpart.

Over the last two decades characteristic-based upwind methods have established themselves as the methods of choice for computing the convective fluxes in the Euler and Navier-Stokes equations. Many investigations on numerical methods for compressible flows have focused on the construction of approximate solutions to the Riemann problem, primarily motivated by the fact that exact solutions are expensive to compute. Most of the existing approximate solutions are capable of giving good solutions to one-dimensional inviscid flows. However, numerical experience has shown that a number of problems have surfaced in more demanding situations, such as in flows with strong shocks or expansions, or in complex multidimensional flows. Linearised approximate Riemann solvers, such as Roe’s flux-difference scheme, are especially prone to such failings. Although some failings are easily cured using so-called entropy corrections, these modifications usually have undesired side-effects, such as rendering the modified solver incapable of recognizing isolated discontinuities, which would otherwise have been its main advantage in viscous flows. In this work, the HLLC scheme developed by Toro et al.<sup>20–21</sup> has been used for computing the inviscid fluxes. HLLC scheme is attractive because of its robustness, conceptual simplicity, and ease of coding. HLLC scheme seems to be a promising method for compressible viscous flows, due to its positivity-preserving property, and the fact that the entropy condition is strongly enforced without the need for any additional modifications. Furthermore, HLLC scheme can easily and simply accommodate general equations of state, and the extension of the HLLC scheme to low Mach number flows in conjunction with time-derivative preconditioning is straightforward and simple<sup>22</sup>. HLLC scheme has been successfully used to compute compressible viscous and turbulent flows on structured grids<sup>21</sup>, and on unstructured grids<sup>5</sup>.

Development of computationally efficient algorithms for high Reynolds number viscous flow simulations on highly stretched unstructured grids remains one of the unresolved issues in computational fluid dynamics. Due to the large differences between the convective and diffusive time scales, high Reynolds number flows produce very stiff systems of equations. This presents a severe challenge to the time advancement procedure. By itself, explicit, multi-stage time advancement is not a computationally viable alternative. A multigrid strategy or an implicit temporal discretization is required in order to speed up convergence. In general, implicit methods can outper-

form their explicit counterparts by a factor of 10 or even more. Unfortunately, this performance is usually achieved at the expense of memory increase, as some efficient implicit methods may need up to an order of magnitude more storage than the explicit methods. This is mainly due to the fact that implicit methods usually require the storage of the left-hand-side Jacobian matrix. Any implicit methods requiring the storage of the Jacobian matrix would be impractical, if not impossible, to use to perform turbulent simulations involving complex, realistic aerodynamic configurations, where millions of mesh points are necessary to represent such engineering-type configurations accurately. The authors have developed a fast, matrix-free implicit method, GMRES+LU-SGS<sup>6</sup>, for solving compressible Euler and Navier-Stokes equations on unstructured grids. The developed GMRES+LU-SGS method has proven to be very effective for accelerating the convergence to both steady,<sup>6</sup> unsteady,<sup>7</sup> and low Mach number<sup>8</sup> flow problems.

Despite the use of the current efficient GMRES+LU-SGS method to solve the system of linear equations at each time-steps, the overall computational requirements are still very substantial. As a consequence, practical computations for complex geometries require the use of parallel computing to produce results within an acceptable timescale. This is true both for production calculations and during the code development. The parallelization of the matrix-free GMRES+LU-SGS implicit method is achieved using OpenMP compiler directives on shared-memory, cache-based parallel machines<sup>9</sup>. This parallelization is based on a special grid renumbering technique rather than the traditional method of partitioning the computational domain. This renumbering technique helps to avoid inter-processor data dependencies, cache-misses, and cache-line overwrite while allowing pipelining. The resulting code can be used with maximum efficiency and without modifications on traditional scalar computers, vector supercomputers, and shared-memory parallel systems.

## 4. COMPUTATIONAL RESULTS

### A. DLR-F4 configuration

The developed unstructured grid solver has been used to compute the test cases for the first AIAA Drag Prediction Workshop<sup>23</sup> held in Anaheim, CA June 2001. The workshop challenge was to compute the lift, drag, and pitching moment for the DLR-F4 wing-body configuration for different sets of conditions. For all cases the free stream Mach number is 0.75, and the Reynolds number is 3 millions. The mandatory calculations for the Drag Prediction Workshop were performed using the standard unstructured nodal grid, which contains 9,650,674 elements, 1,641,451 points, and 48,339 boundary points, as shown in Figure 1a.

All computations were initiated as a uniform flow at freestream conditions, and advanced with a CFL number of 200. The relative  $L_2$  norm of the density residual is taken as the criterion for convergence history. The solution tolerance for GMRES was set to 0.1 with 10 search directions and 20 iterations. We observed that during the first few time steps, more iterations are required to solve the system of the linear equations: even 20 iterations can not guarantee that the stopping criterion will be satisfied for some cases. However, it takes less than 20 iterations to solve the linear equations at a later time, and global convergence is not affected by a lack of linear system convergence during the first few time steps. All computations were performed on a SGI origin 2000 (400MHz) computer and required 4 GB memory and about 7 hours on 16 processors for 1000 time-steps. Note that convergence in the lift and drag is obtained in as little as 500 time steps for all cases.

The first test case is a single point at  $C_L=0.5$ . The computed pressure contours displayed in Fig. 1b, clearly show good resolution of the upper surface shock. Figs. 1c-h show the comparison of experimental data<sup>23</sup> and computed pressure coefficient distributions at six spanwise stations, respectively. The results obtained compare closely with the experimental data, although the upper surface pressure peak is lower than the experimental data, and the post-shock Mach number is too high (as obtained by most of the participants in the DPW). The convergence histories for density residual, lift, pressure, and skin-friction drag coefficients are shown in Figs. 1i-j, respectively, where one can see that force coefficients converge in 600 time steps. Table 1 summarizes the results obtained for case 1 by the experiments, drag prediction workshop participants, and present computation. Although there is a considerable amount of scatter in the data obtained by the drag prediction workshop, our computational results are close to the average data, especially for drag and pitching moment.

Table 1. Comparison of computational results with experimental data and Drag Prediction Workshop data for case 1

Data	$\alpha$	$C_L$	$C_D$	$C_M$
ONERA	0.192	0.50	0.02896	-0.1260
NLR	0.153	0.50	0.02889	-0.1301
DRA	0.179	0.50	0.02793	-0.1371
Workshop(Ave)	-0.237	0.5002	0.03037	-0.1559
Workshop(Min)	-1.000	0.4980	0.02257	-0.2276
Workshop(Max)	1.223	0.5060	0.04998	0.0481
Present	-0.002	0.5009	0.03058	-0.1513

The second test case involves the computation of the drag polar at angles of attack from -3 to 2 degrees in increments of 1 degree. The convergence histories for density residual, and lift coefficient are

shown in Fig. 1k, where one can see that solutions are converged to engineering accuracy (a decrease of three orders-of-magnitude in the  $L_2$  norm of the density residual) in about 500 time steps. Lift and drag coefficient convergence was obtained in 500 time steps as well. The computed lift coefficients versus angles of attack, the lift coefficients versus the drag coefficients, and the pitching moment coefficients versus the lift coefficients along with the experimental data are shown in Figs. 1l-1n, respectively. Our computations yield a higher  $C_L$  at a given angle of attack than the wind tunnel data. Despite the large scatter in the drag polars obtained by the Drag Prediction Workshop, our computational results compare relatively well with experimental data.

### B. DLR-F6 configuration

The computed results are presented here for the test cases in the 2nd AIAA Drag Prediction Workshop<sup>24</sup> held in Orlando, FL June 2003. The chosen configuration, denoted as DLR-F6, consists of wing-body geometry without or with a conventional nacelle. All computations were performed on the NAVO IBM Cluster 1600 (1.3 GHz Power 4) computer and required less than 8 Gbytes memory and less than 12 hours of CPU on 8 processors. Although the Drag Prediction Workshop specified several mandatory and optional cases, only the mandatory cases were computed in this work. For all cases the free stream Mach number is 0.75, and the Reynolds number based on reference chord of 14.12cm is 3 millions.

The first case is a single point at a prescribed lift coefficient of 0.5. In order to test the robustness of the present method on grids generated by different grid generators, the grid convergence study was performed using the coarse grid provided by NASA LARC as our coarse grid, the coarse grid provided by Swansea as our medium grid, and the coarse grid by DLR as our fine grid. Table 2 shows the grid size and computed results for the wing-body configuration for case 1 with the three different grids. The comparison of lift and drag coefficients with the experimental data is shown in Figs. 2a-b, respectively. Although there is a considerable amount of scatter in the data obtained by the drag prediction workshop, our computational results are close to the average data. The computed pressure contours on the medium mesh is displayed in Fig. 2c. Figs. 2d-k show the comparison of experimental data<sup>24</sup> and computed pressure coefficient distributions at eight spanwise stations, respectively. The results obtained compare closely with the experimental data, although the post-shock Mach number is too high (as obtained by most of the participants in the DPW). Table 3 shows the grid size and computed results for the wing-body-pylon-nacelle configuration for case 1 with the three different grids. The com-

parison of lift and drag coefficients with the experimental data is shown in Figs. 2l-m, respectively. The computed pressure contours on the medium mesh is displayed in Fig. 2n. Figs. 2o-v show the comparison of experimental data<sup>24</sup> and computed pressure coefficient distributions at eight spanwise stations, respectively. The comparison of computed results with the experimental data is reasonably good, although the upper surface pressure peak is higher than the experimental data, and the shock position is overpredicted especially in the wing tip sections.

Table 2. Case 1: Wing/body Configuration

Grid Size	$\alpha$	$C_L$	$C_D$	$C_M$
1,121,301	0.376	0.499	0.03165	-0.1244
1,779,420	0.280	0.500	0.03038	-0.1281
2,390,716	0.275	0.499	0.03034	-0.1332

Table 3. Case 1: Wing/body/pylon/nacelle Configuration

Grid Size	$\alpha$	$C_L$	$C_D$	$C_M$
1,827,470	0.950	0.497	0.03719	-0.1205
2,419,388	0.843	0.498	0.03658	-0.1216
3,682,535	0.800	0.501	0.03631	-0.1242

The second case involves the computation of the drag polar at angles of attack of -3, -2, -1.5, -1, 0, 1, and 1.5 degrees. The calculations were performed on the medium mesh. The convergence histories of density residual, and lift coefficient for the wing-body configuration are shown in Figs. 2w-x respectively, where one can see that solutions are converged to engineering accuracy (a decrease of three orders-of-magnitude in the  $L_2$  norm of the density residual) in about 800 time steps. Note that slow convergence for wing-body-nacelle-pylon configuration at lower angle of attack has been observed, this is due to the fact that the flow separation occurs near the wing root region, and there is not enough grid resolution for the coarse mesh used in our computation. The computed lift coefficients versus angles of attack, the lift coefficients versus the drag coefficients, and the pitching moment coefficients versus the lift coefficients along with the experimental data for both wing-body and wing-body-pylon-nacelle configurations are shown in Figs. 2y-z, respectively. Our computations yield a higher  $C_L$  at a given angle of attack than the wind tunnel data. Despite the large scatter in the drag polars obtained by the Drag Prediction Workshop, our computational results compare relatively well with experimental data.

## 5. CONCLUSIONS

A numerical method has been presented to compute three-dimensional compressible turbulent flows for complex geometries using a one-equation turbulence model on unstructured grids. The method uses containment dual control volume to discretize the in-

viscid fluxes to achieve the dramatic improvement in accuracy on a highly stretched tetrahedral mesh and the matrix-free implicit GMRES+LU-SGS method to achieve the fast convergency. The developed method has been applied to compute drags in the transonic regime for both DLR-F4 and DLR-F6 configurations. The results obtained are in good agreement with the experimental data, demonstrating good drag predictive ability of the present method. It is concluded that with the rapid convergence of the present implicit method together with the parallel implementation on multi-processors computers, the turnaround in a matter of hours for numerical simulation of high Reynolds number turbulent flows around complex geometries has become a reality.

## 6. REFERENCES

- <sup>1</sup>V. Parthasarathy, and Y. Kallinderis, "Adaptive Prismatic-Tetrahedral Grid Refinement and Redistribution for Viscous Flows", *AIAA J.*, Vol. 34, pp. 707-716, 1996.
- <sup>2</sup>K. Nakahashi, D. Sharov, S. Kano, and M. Kodera, "Application of Unstructured Hybrid Grid Method to High-Reynolds Number Viscous Flows", *International Journal for Numerical Methods in Fluids*, Vol. 31, pp. 97-111, 1999.
- <sup>3</sup>A. Haselbacher, J. J. McGuirk, and G. J. Page, "Finite-Volume Discretization Aspects for Viscous Flows for Mixed Unstructured Meshes", *AIAA Journal*, Vol. 37, pp. 177-184, 1999.
- <sup>4</sup>D. Sharov, H. Luo, J.D. Baum, and R. Löhner, "Unstructured Navier-Stokes Grid Generation at Corners and Ridges", *International Journal for Numerical Methods in Fluids*, Vol. 43, pp. 717-728, 2003.
- <sup>5</sup>H. Luo, D. Sharov, J.D. Baum, and R. Löhner, "On the Computation of Compressible Turbulent Flows on Unstructured Grids", *International Journal for Computational Fluid Dynamics*, Vol. 14, pp. 253-270, 2001.
- <sup>6</sup>H. Luo, J.D. Baum, and R. Löhner, "A Fast, Matrix-free Implicit Method for Compressible Flows on Unstructured Grids", *Journal of Computational Physics*, Vol. 146, 1998.
- <sup>7</sup>H. Luo, J.D. Baum, and R. Löhner, "An Accurate, Fast, Matrix-free Implicit Method for Computing Unsteady Flows on Unstructured Grids", *Computers & Fluids* Vol. 30, No. 2, pp. 137-159, 2001.
- <sup>8</sup>H. Luo, J. D. Baum, and R. Löhner, "A Fast, Matrix-free Implicit Method for Computing Low Mach Number Flows on Unstructured Grids", *International Journal of Computational Fluid Dynamics* Vol. 14, pp. 133-157, 2001.
- <sup>9</sup>H. Luo, D. Sharov, J. D. Baum, and R. Löhner, "Parallel Unstructured Grid GMRES+LU-SGS Method for Turbulent Flows", *AIAA Paper* 2003-0273, 2003.
- <sup>10</sup>P.R. Spalart, and S.R. Allmaras, "A One-equations Turbulence Model for Aerodynamic Flows", *AIAA Paper* 92-0439, 1992.
- <sup>11</sup>M. Aftosmis, D. Gaitonde, and T. S. Tavares, "On the Accuracy, Stability, and Monotonicity of Various Reconstruction Algorithms for Unstructured Meshes", *AIAA Paper* 94-0415, 1994.
- <sup>12</sup>C. Viozat, C. Held, K. Mer, and A. Dervieux, "On Vertex-Centered Unstructured Finite-Volume Methods for Stretched Anisotropic Triangulations", *INRIA Report de Recherche* No. 3464, 1998.
- <sup>13</sup>C. P. Rumsey, B. van Leer, and P. L. Roe, "A Multidimensional Flux Function with Applications to the Euler and Navier-Stokes Equations", *Journal of Computational Physics*, Vol. 105, No. 2, pp. 306-323, 1993.
- <sup>14</sup>P. L. Roe, "Discrete Models for the Numerical Analysis of Time-Dependent Multidimensional Gas Dynamics", *Journal of Computational Physics*, Vol. 63, No. 2, pp. 458-476, 1986.
- <sup>15</sup>H. Deconinck, C. Hirsch, and J. Peuteman, "Characteristic Decomposition Methods for the Euler Equations", *Lecture Notes in Physics*, Vol. 6, pp. 216-221, 1986.
- <sup>16</sup>P. Van Ransbeeck, and C. Hirsch, "New Upwind Dissipation Models with a Multidimensional Approach", *AIAA Paper* 93-3304, 1993.
- <sup>17</sup>I. H. Parpia, and D. J. Michalek, "A Nearly-Monotone Genuinely Multidimensional Scheme for the Euler Equations", *AIAA Paper* 92-0325, 1995.
- <sup>18</sup>X. D. Zhang, J. Y. Trépanier, M. Reggio, A. Benmeddour, and R. Camaero, "Grid Influence on Upwind Schemes for the Euler and Navier-Stokes Equations", *AIAA Journal*, Vol. 34, No. 4, pp. 717-727, 1996.
- <sup>19</sup>T. J. Barth, and S. W. Linton, "An unstructured Mesh Newton Solver for Compressible Turbulent Flows and Its Parallel Implementation", *AIAA Paper* 95-0221, 1995.
- <sup>20</sup>Toro, E.F., Spruce, M., and Speares, W., "Restoration of the Contact Surface in the HLL Riemann Solver", *Shock Waves*, 4, 25, 1994.
- <sup>21</sup>P. Batten, M. A. Leschziner, and U. C. Goldberg, "Average-State Jacobians and Implicit Methods for Compressible Viscous and Turbulent Flows", *Journal of Computational Physics*, 137, pp. 38-78, 1997.
- <sup>22</sup>H. Luo, J. D. Baum, and R. Löhner, "Extension of HLLC Scheme for Flows at All Speeds", *AIAA Paper* 2003-3840, 2003.
- <sup>23</sup>1st AIAA Drag Prediction Workshop. Anaheim, CA. <http://www.aiaa.org/tc/apa/dragpredworkshop/dpw.html>, June 2001.
- <sup>24</sup>2nd AIAA Drag Prediction Workshop. Orlando, FL. <http://aaac.larc.nasa.gov/tsab/cfdlarc/aiaa-dwp/index.html> June 2003.

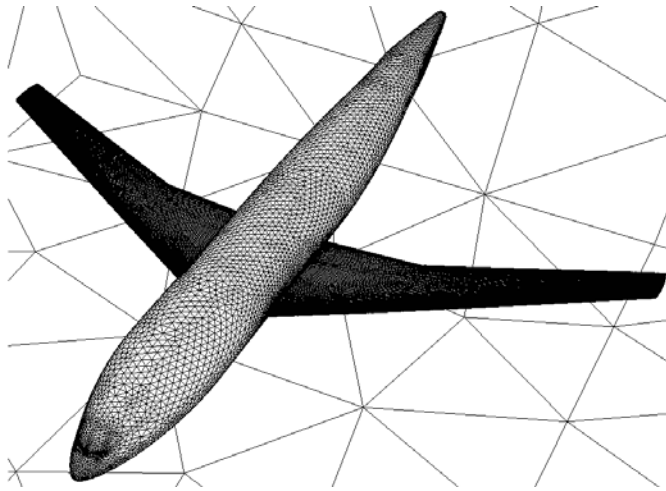


Fig. 1a: Unstructured surface mesh used for computing turbulent flow past DLR-F4 configuration (nelem=9,650,674, npoin=1,641,451, nboun=48,339).

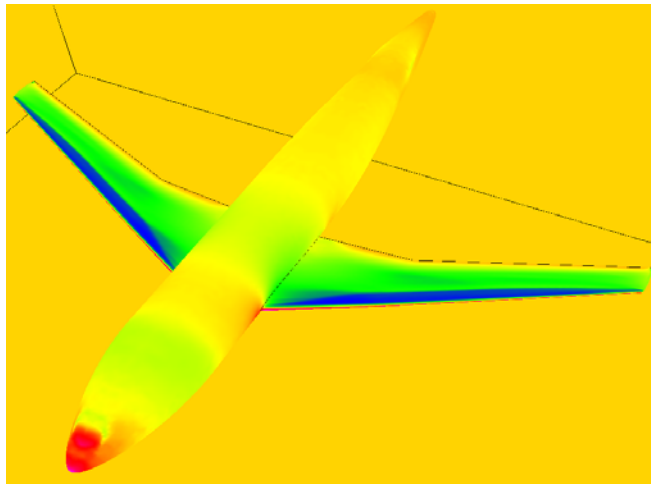


Fig. 1b: Computed pressure contours on the surface of DLR-F4 configuration at  $M_\infty = 0.75$ ,  $\alpha = -0.002^\circ$ , and  $Re=3,000,000$ .

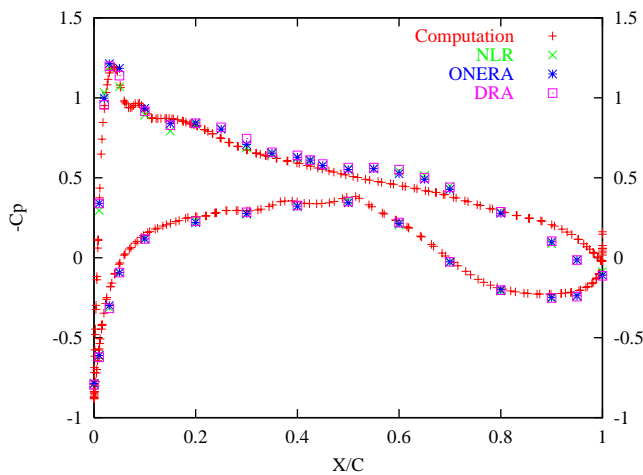


Fig. 1c: Comparison between experimental and computed pressure coefficient distributions for wing section at 18.5% semispan.

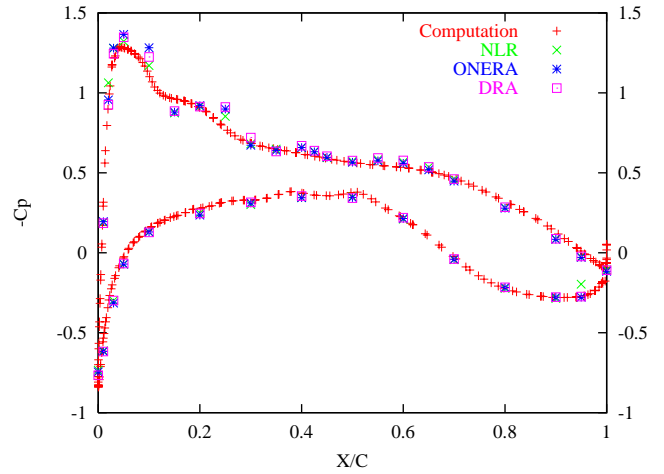


Fig. 1d: Comparison between experimental and computed pressure coefficient distributions for wing section at 23.8% semispan.

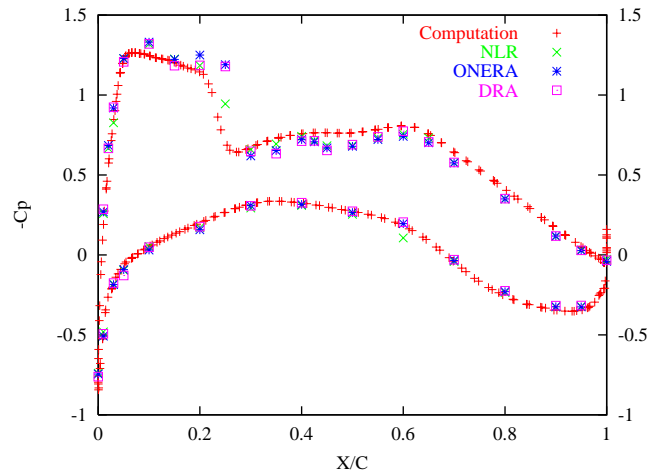


Fig. 1e: Comparison between experimental and computed pressure coefficient distributions for wing section at 41.1% semispan.

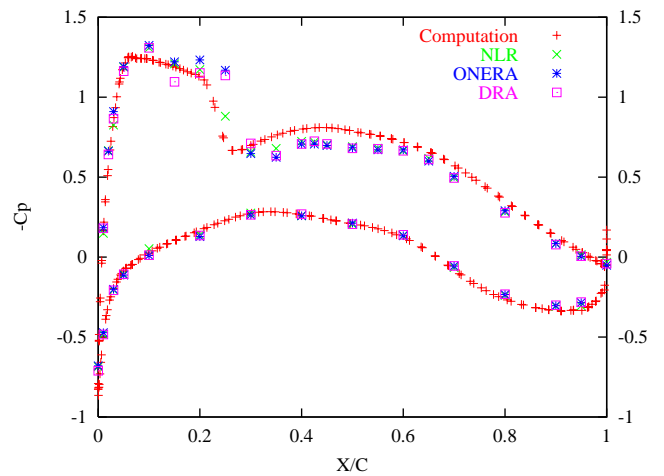


Fig. 1f: Comparison between experimental and computed pressure coefficient distributions for wing section at 51.4% semispan.

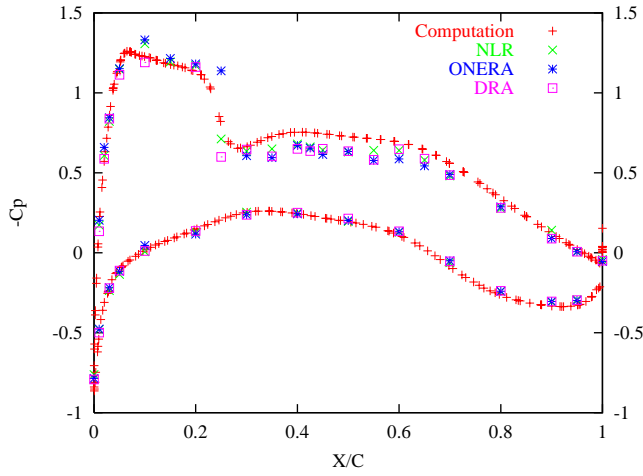


Fig. 1g: Comparison between experimental and computed pressure coefficient distributions for wing section at 63.8% semispan.

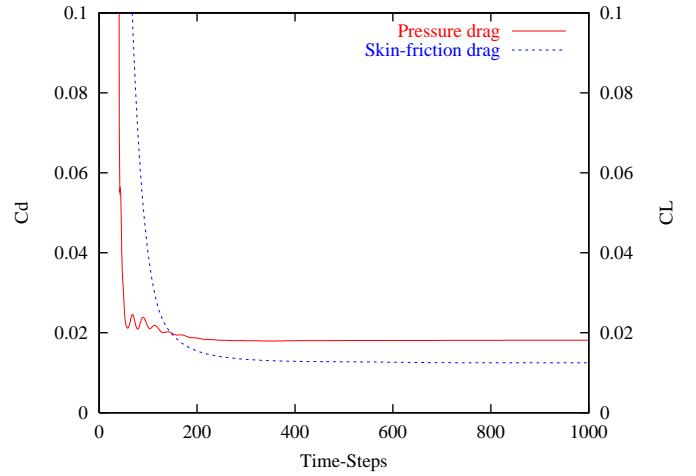


Fig. 1j: Pressure and skin friction drag coefficient convergence history for DLR-F4 configuration at  $M_\infty = 0.75$ ,  $C_l = 0.5009$ ,  $\alpha = -0.002^\circ$ , and  $Re=3,000,000$ .

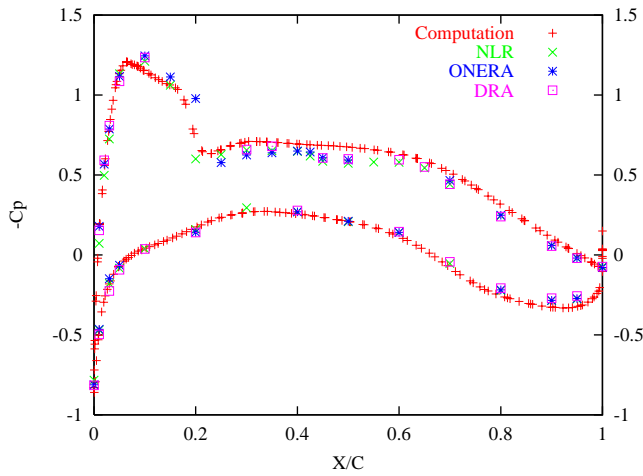


Fig. 1h: Comparison between experimental and computed pressure coefficient distributions for wing section at 84.7% semispan.

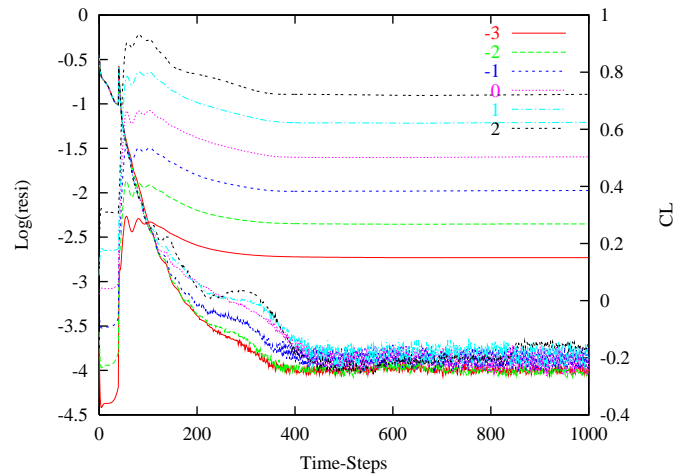


Fig. 1k: Density residual and lift coefficient convergence history for DLR-F4 configuration at different angles of attack at  $M_\infty = 0.75$ , and  $Re=3,000,000$ .

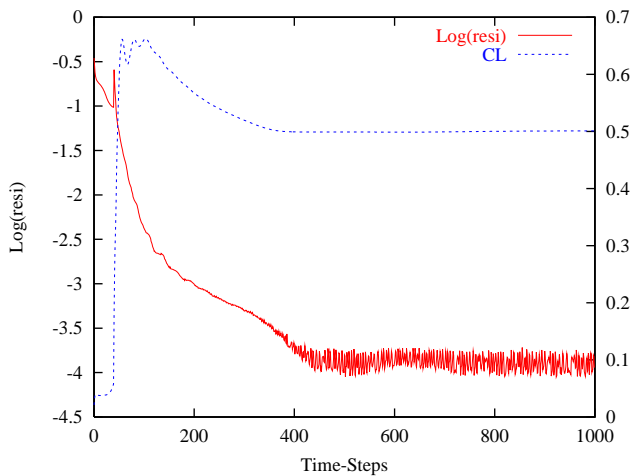


Fig. 1i: Density residual and lift coefficient convergence history for DLR-F4 configuration at  $M_\infty = 0.75$ ,  $C_l = 0.5009$ ,  $\alpha = -0.002^\circ$ , and  $Re=3,000,000$ .

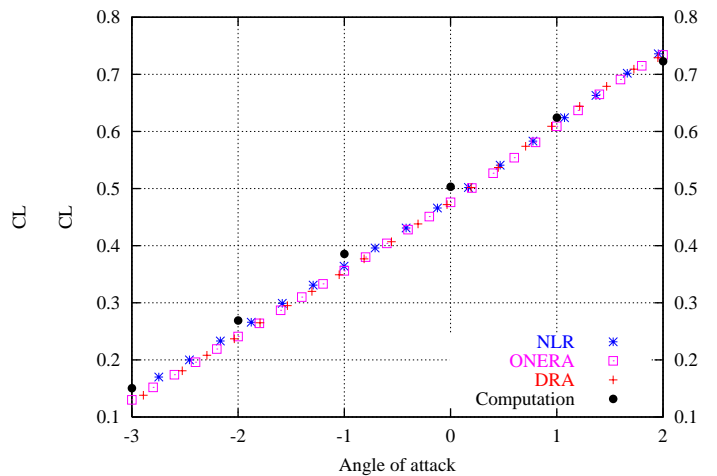


Fig. 1l: Comparison of computed lift coefficient and experimental data for DLR-F4 configuration at different angles of attack at  $M_\infty = 0.75$ , and  $Re=3,000,000$ .

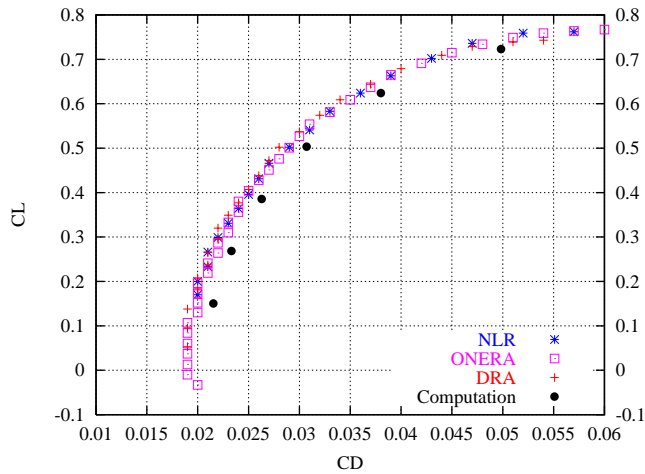


Fig. 1m: Comparison of computed and experimental drag polar for DLR-F4 configuration at  $M_\infty = 0.75$ , and  $Re=3,000,000$ .

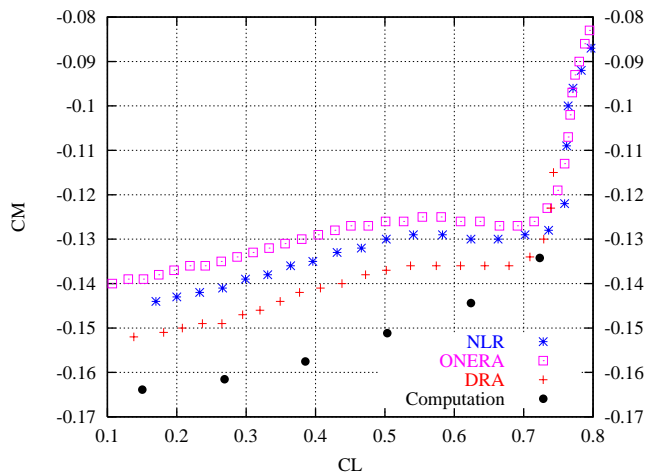


Fig. 1n: Comparison of computed and experimental pitching moment coefficient for DLR-F4 configuration at  $M_\infty = 0.75$ , and  $Re=3,000,000$ .

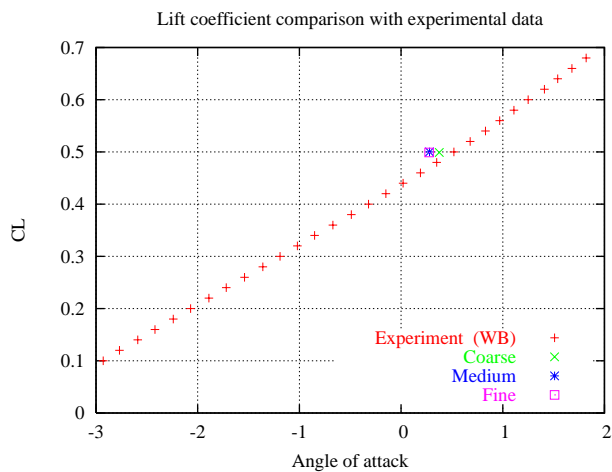


Fig. 2a: Comparison of computed lift coefficient and experimental data for DLR-F6 wing-body configuration at  $M_\infty = 0.75$ , and  $Re=3,000,000$ .

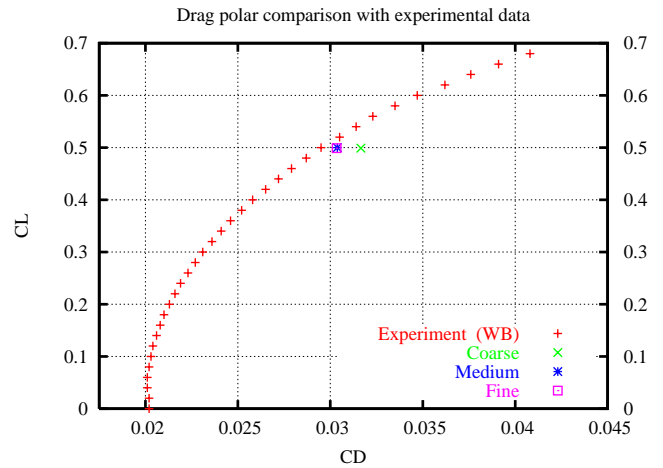


Fig. 2b: Comparison of computed and experimental drag polar for DLR-F6 wing-body configuration at  $M_\infty = 0.75$ , and  $Re=3,000,000$ .

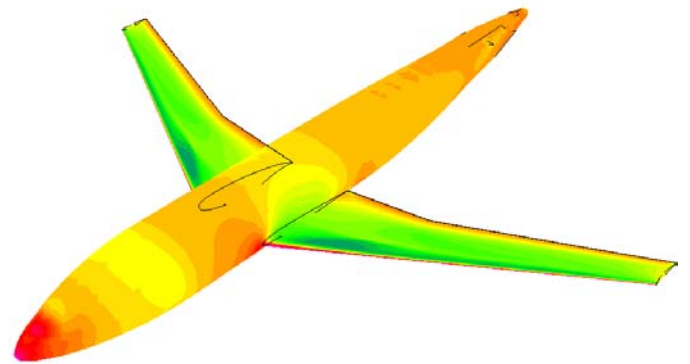


Fig. 2c: Computed pressure contours on the surface of DLR-F6 wing-body configuration at  $M_\infty = 0.75$ ,  $C_L=0.5$ , and  $Re=3,000,000$ .

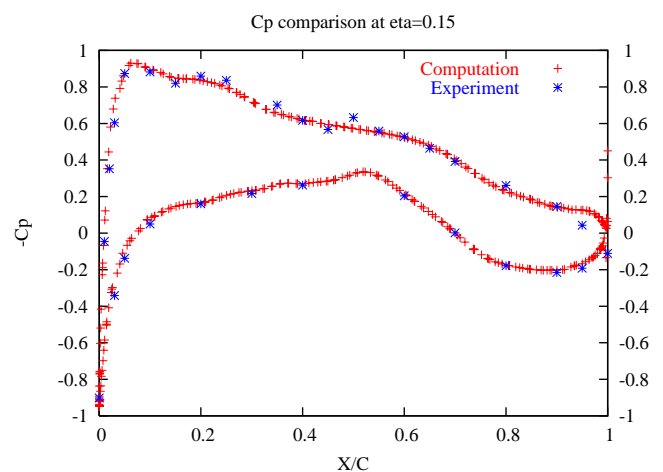


Fig. 2d: Comparison between experimental and computed pressure coefficient distributions for wing section at 15% semispan.

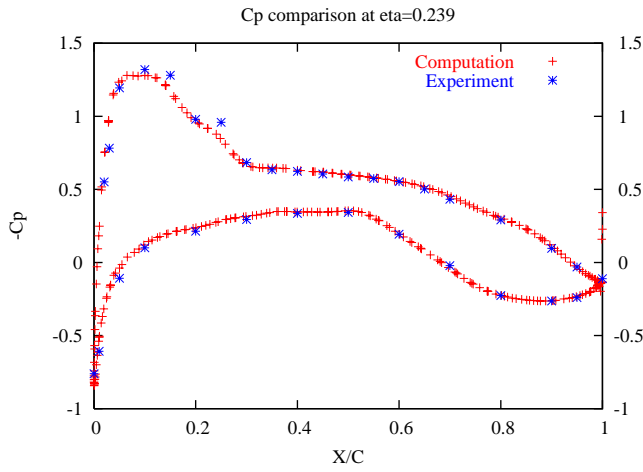


Fig. 2e: Comparison between experimental and computed pressure coefficient distributions for wing section at 23.9% semispan.

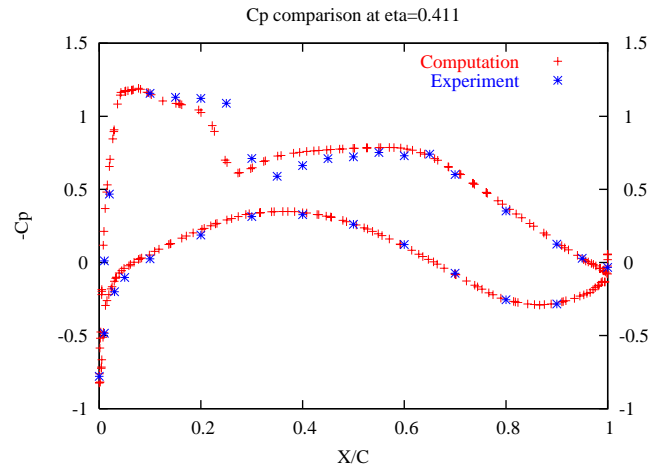


Fig. 2h: Comparison between experimental and computed pressure coefficient distributions for wing section at 41.1% semispan.

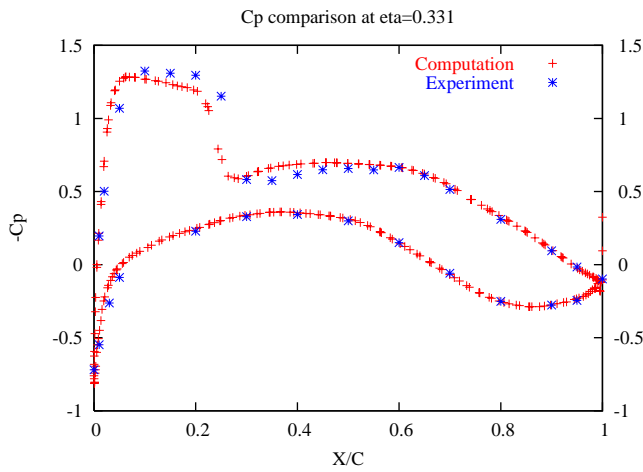


Fig. 2f: Comparison between experimental and computed pressure coefficient distributions for wing section at 33.1% semispan.

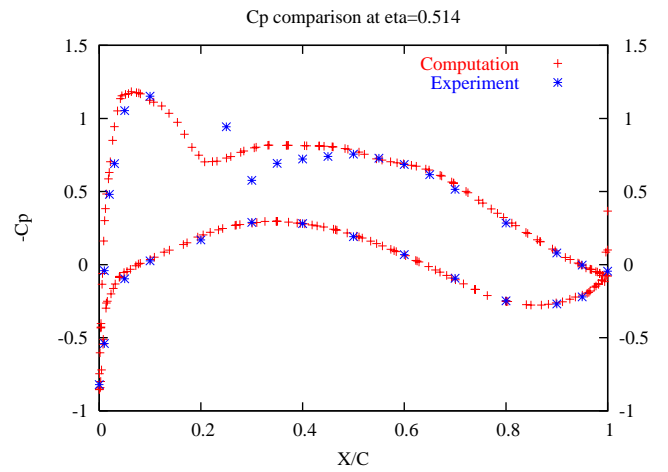


Fig. 2i: Comparison between experimental and computed pressure coefficient distributions for wing section at 51.4% semispan.

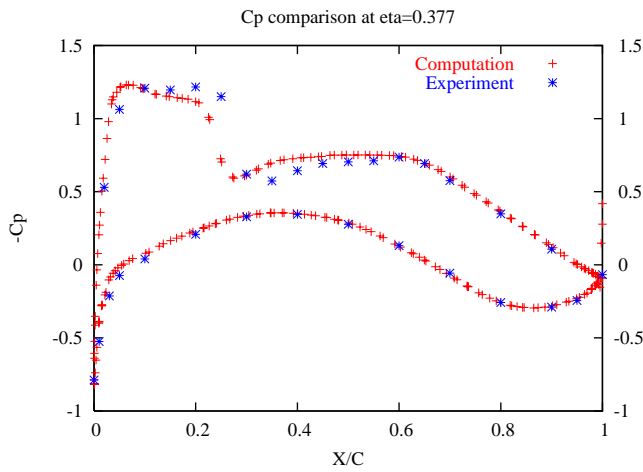


Fig. 2g: Comparison between experimental and computed pressure coefficient distributions for wing section at 37.7% semispan.

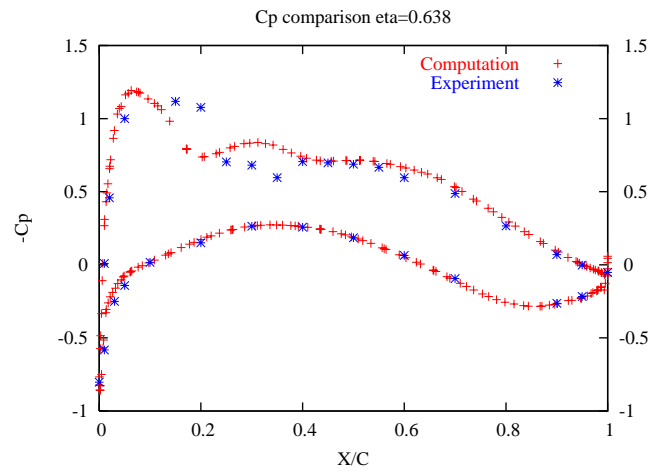


Fig. 2j: Comparison between experimental and computed pressure coefficient distributions for wing section at 63.8% semispan.

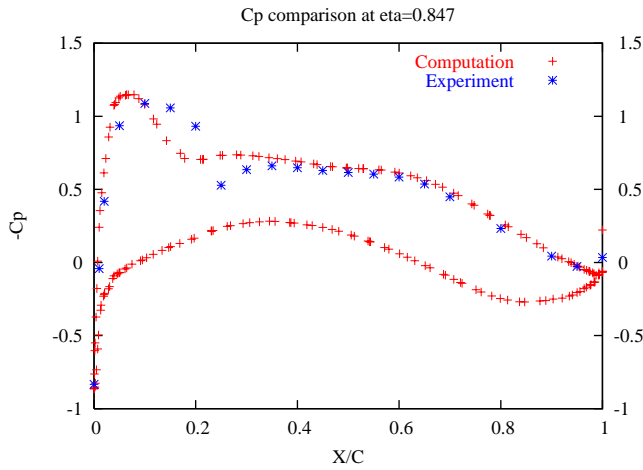


Fig. 2k: Comparison between experimental and computed pressure coefficient distributions for wing section at 84.7% semispan.

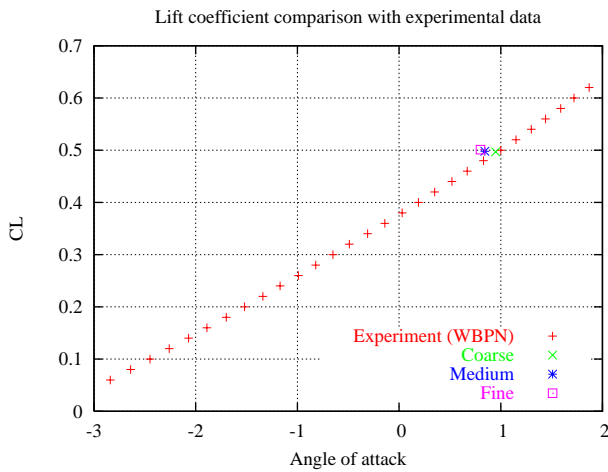


Fig. 2l: Comparison of computed lift coefficient and experimental data for DLR-F6 wing-body-pylon-nacelle configuration at  $M_\infty = 0.75$ , and  $Re=3,000,000$ .

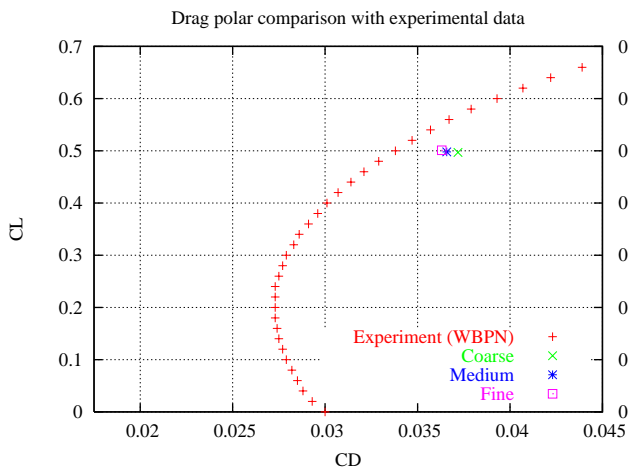


Fig. 2m: Comparison of computed and experimental drag polar for DLR-F6 wing-body-pylon-nacelle configuration at  $M_\infty = 0.75$ , and  $Re=3,000,000$ .

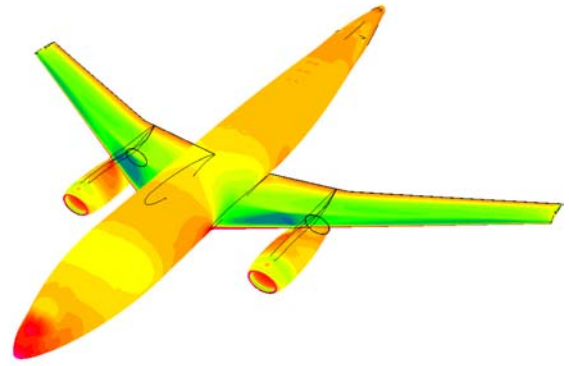


Fig. 2n: Computed pressure contours on the surface of DLR-F6 wing-body configuration at  $M_\infty = 0.75$ ,  $C_L=0.5$ , and  $Re=3,000,000$ .

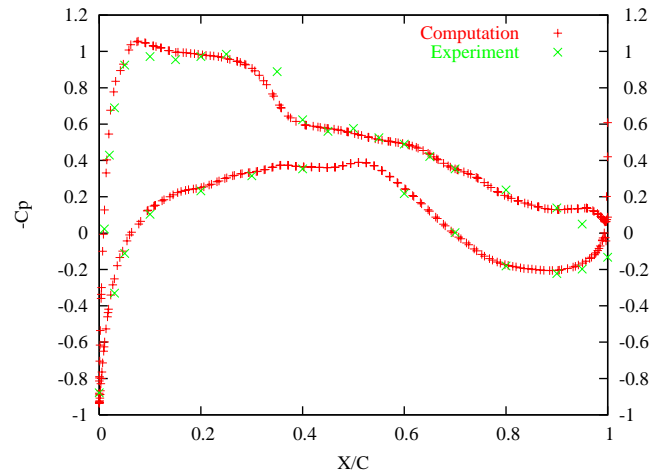


Fig. 2o: Comparison between experimental and computed pressure coefficient distributions for wing section at 15.0% semispan.

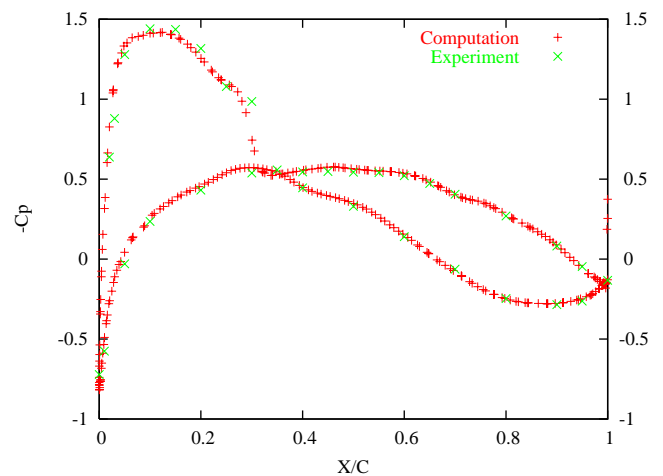


Fig. 2p: Comparison between experimental and computed pressure coefficient distributions for wing section at 23.9% semispan.

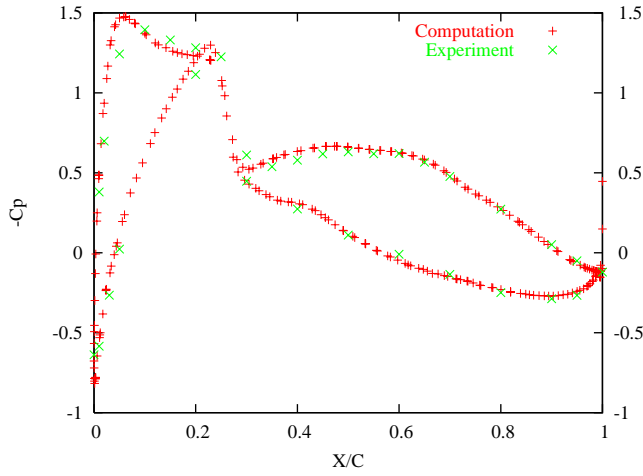


Fig. 2q: Comparison between experimental and computed pressure coefficient distributions for wing section at 33.1% semispan.

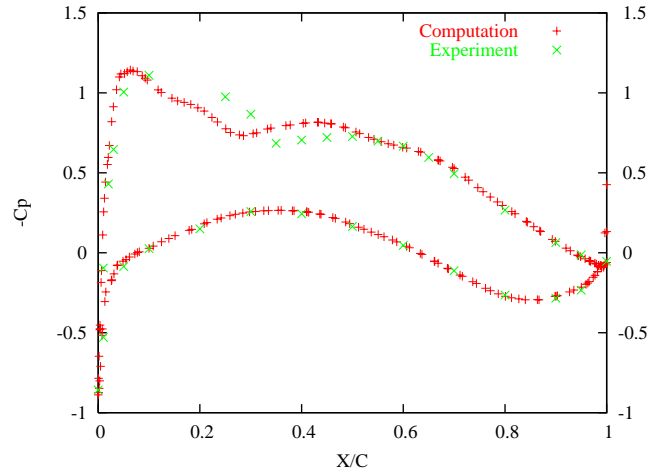


Fig. 2t: Comparison between experimental and computed pressure coefficient distributions for wing section at 51.4% semispan.

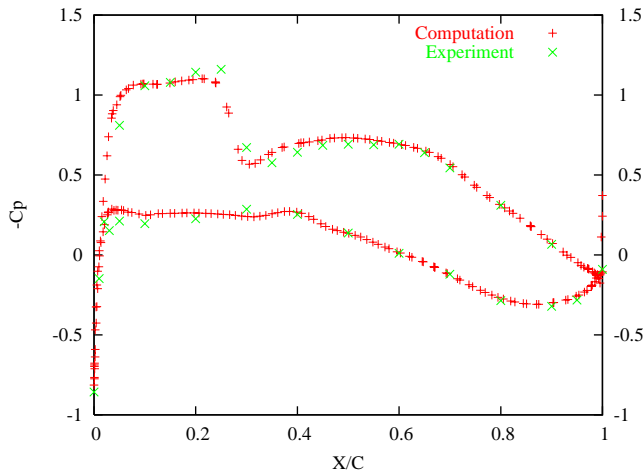


Fig. 2r: Comparison between experimental and computed pressure coefficient distributions for wing section at 37.7% semispan.

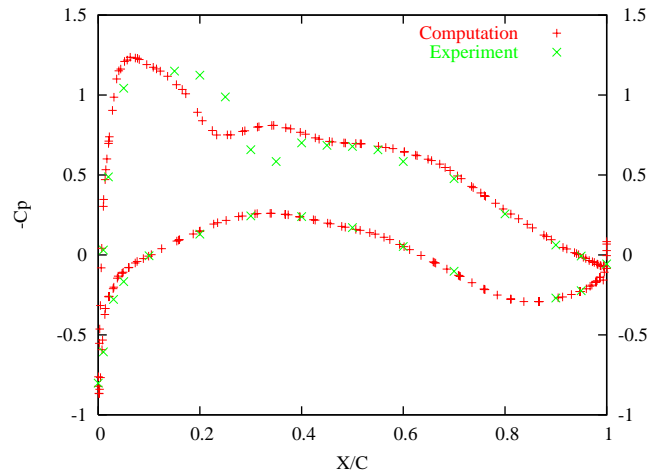


Fig. 2u: Comparison between experimental and computed pressure coefficient distributions for wing section at 63.8% semispan.

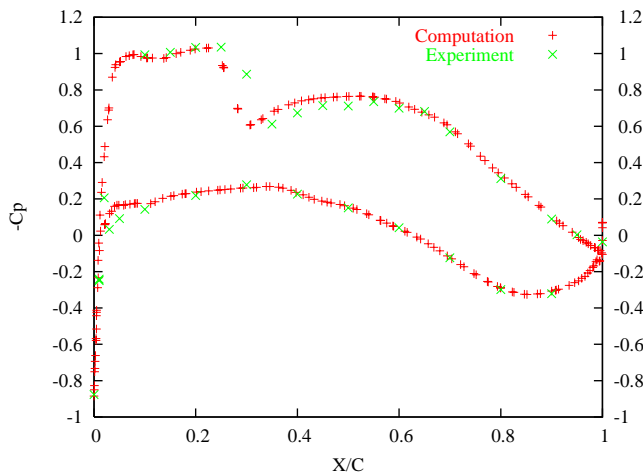


Fig. 2s: Comparison between experimental and computed pressure coefficient distributions for wing section at 41.1% semispan.

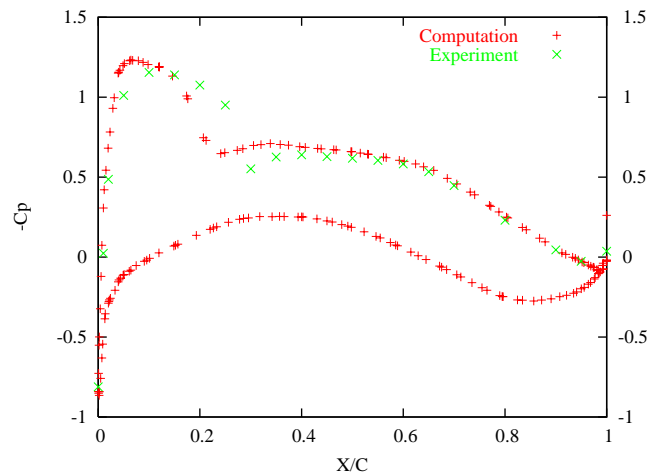


Fig. 2v: Comparison between experimental and computed pressure coefficient distributions for wing section at 84.7% semispan.

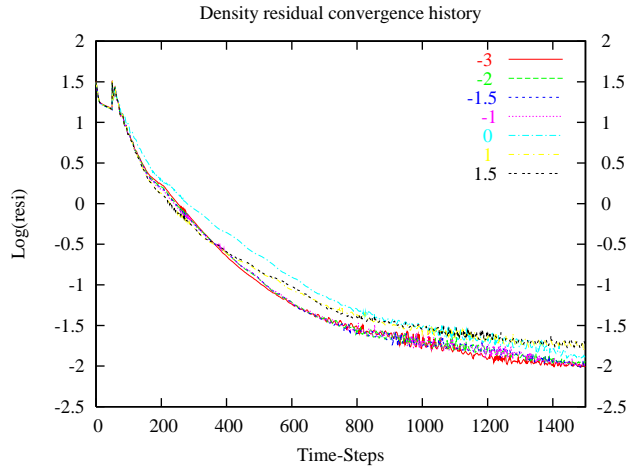


Fig. 2w: Density residual and lift coefficient convergence history for DLR-F6 wing/body configuration at different angles of attack at  $M_\infty = 0.75$ , and  $Re=3,000,000$ .

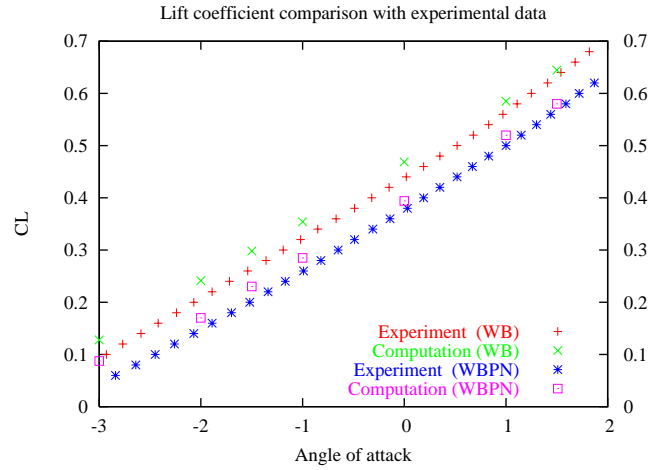


Fig. 2y: Comparison of computed lift coefficient and experimental data for DLR-F6 configuration at different angles of attack and at  $M_\infty = 0.75$ , and  $Re=3,000,000$ .

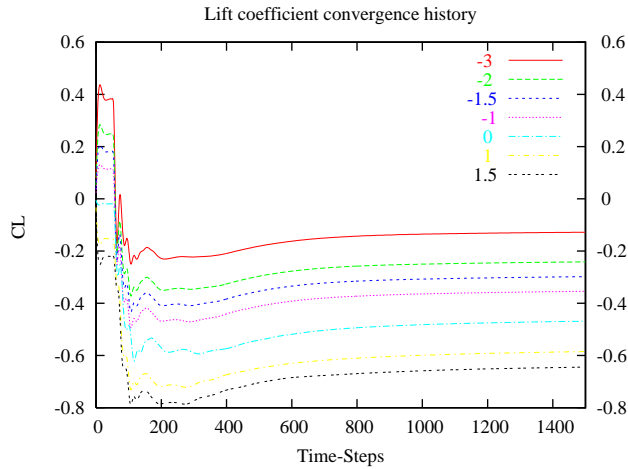


Fig. 2x: Density residual and lift coefficient convergence history for DLR-F4 wing/body configuration at different angles of attack at  $M_\infty = 0.75$ , and  $Re=3,000,000$ .

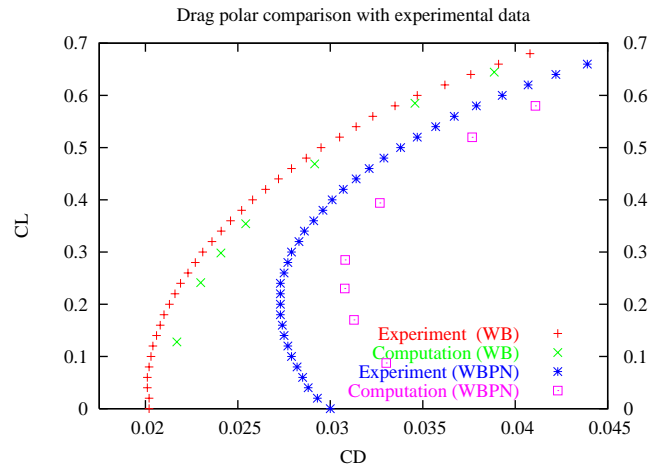


Fig. 2z: Comparison of computed and experimental drag polar for DLR-F6 configuration at  $M_\infty = 0.75$ , and  $Re=3,000,000$ .